ACS APPLIED MATERIALS & INTERFACES

Research Article

Cite This: ACS Appl. Mater. Interfaces 2019, 11, 30968−30976

www.acsami.org

Ethanol Electrooxidation Catalyzed by Tungsten Core@Palladium Shell Nanoparticles

Yang Yang,[†] Minghua Tian,[†] Qiaoxia Li,*[,†,‡,§] Yulin Min,[†] Qunjie Xu,[†,§] and Shaowei Chen*[,‡]

[†]Shanghai Key Laboratory of Materials Protection and Advanced Materials in Electric Power, College of Environmental and Chemical Engineering, Shanghai University of Electric Power, 2588 Changyang Road, Yangpu District, Shanghai 200090, China

[‡]Department of Chemistry and Biochemistry, University of California, Santa Cruz, 1156 High Street, Santa Cruz, California 95064, United States

[§]Shanghai Institute of Pollution Control and Ecological Security, Shanghai 200090, China

Supporting Information

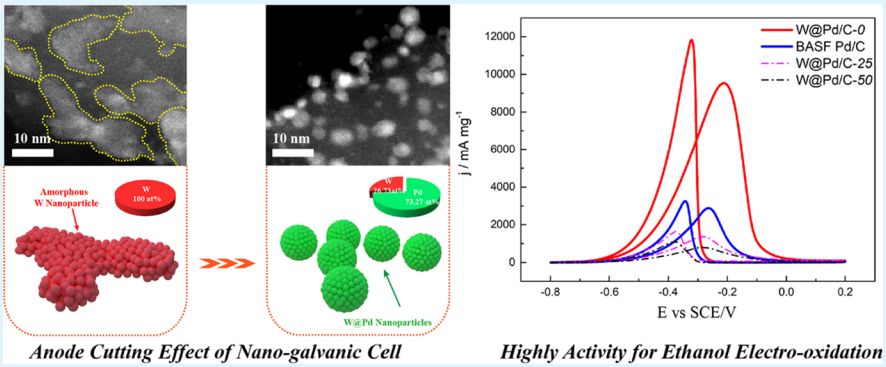

ABSTRACT: Bimetallic nanostructures represent effective electrocatalysts toward a number of important reactions. In the present study, carbon-supported palladium−tungsten alloy nanoparticles with a quasi-tungsten core@palladium shell structure (W@Pd/C) were synthesized by a galvanic replacement reaction of amorphous tungsten nanoparticles with Pd(II) at different temperatures (0, 25, and 50 °C), and exhibited apparent electrocatalytic activity toward ethanol oxidation reaction (EOR). When the sample was prepared at 0 °C, large amorphous tungsten nanoparticles were etched off and much smaller W@Pd nanoparticles were formed and dispersed rather evenly on the carbon surface whereas at higher reaction temperatures (25 and 50 °C), the W@Pd nanoparticles became agglomerated. The structures of the obtained samples were characterized by a range of experimental tools, including (scanning) transmission electron microscopy, X-ray diffraction, X-ray photoelectron spectroscopy, and electrochemical methods. Among the series, the W@Pd/C sample prepared at 0 °C was observed to exhibit the best EOR performance, with a mass activity (9535.5 mA mg_{Pd}^{-1}) over three times better than that of commercial Pd/C and markedly enhanced stability.

KEYWORDS: *palladium−tungsten nanoparticle, core−shell nanoparticle, galvanic replacement reaction, ethanol oxidation reaction, mass activity*

INTRODUCTION

Small organic molecule fuel cells have been hailed as sustainable energy technologies in recent years because of the enormous potential as high-efficiency portable power devices.[1−4] Of these, direct ethanol fuel cells (DEFCs) represent a viable technology,[5−7] owing largely to the ready availability and ease of transportation of ethanol. The key reaction for DEFCs is ethanol oxidation reaction (EOR) at the anode, which in general follows the dual-pathway mechanism. The C1 pathway involves an adsorbed carbon monoxide (CO_{ad}) intermediate that is further oxidized to CO_2, producing 12 electrons, whereas acetic acid or acetaldehyde is the primary product in the more dominant C2 pathway, where four or two electrons are generated, with CO_{ad}, C1, and C2 hydrocarbon residues being the major intermediates.[8] As CO is formed during EOR, which may poison the catalysts, removal or oxidation of CO from the active sites is critical for enhanced catalytic activity. Therefore, rational design and engineering of highly efficient and durable electrocatalysts has become an area of active interest, with a goal of increasing the C1 to C2 product ratio.[9,10]

Currently, the leading catalysts for EOR are Pd and Pt-based nanoparticles.[11] To reduce the loading and cost, it is of critical significance to increase their utilization efficiency. This can be achieved by, for instance, controlling the nanoparticle size, shape, alloying with a second (nonprecious) metal, etc.[12] In

Received: June 10, 2019
Accepted: August 7, 2019
Published: August 7, 2019

DOI: 10.1021/acsami.9b10156
ACS Appl. Mater. Interfaces 2019, 11, 30968−30976

alkaline media, Pd-based nanoparticles display a high activity and durability for EOR, and alloys or metal oxide hybrids represent a unique system, where synergistic interactions between the different components can manipulate the electronic properties of the noble metals and regulate the bonding interactions with reaction intermediates.[13−20] In fact, Pd-based alloys have been attracting much attention in alkaline EOR. Among these, alloy nanoparticles are of significant interest because (a) the amount of noble metals used (and hence costs) is markedly reduced and (b) the catalytic activity can be further enhanced by the strain, ensemble, and ligand effects between the noble metal and the second metal.[21,22] In recent years, a series of metallic (nonmetallic) elements have indeed been explored to form alloy catalysts with Pd, including noble metals (e.g., Au, Ru, and Ir),[23−27] non-noble metals (e.g., Cu, Ni, and Co),[28−30] and even nonmetallic elements (B and P),[31−34] leading to improved EOR activity.

To further enhance the mass activity of Pd-based nanoparticles toward EOR, one effective strategy is to construct a core@shell structure where a non-noble metal core is encapsulated with a Pd-rich shell by taking advantages of the synergetic interactions between the alloying components and a minimal mass loading of Pd.[35−37] Such core@shell structures can be prepared in a range of methods, such as Cu-mediated deposition, two-step chemical reduction, dealloying, and surface segregation.[30,38−41] In the first two methods, a noble metal shell is produced, but the synthesis process is rather complex, and the yield is low. By contrast, although the utilization of precious metals is not sufficiently high in the final products of the last two methods, mass production of the core@shell catalysts can be readily achieved. The replacement reaction has the advantages of ease of operation and simple experimental conditions.[42] For instance, Xia's group[43] prepared a series of metal nanocrystals by galvanic replacement reactions (GRR), including Ag−Au nanocages,[44] Ag−Au nanoboxes,[45] and Ag−Pd nanoboxes.[46] In another study,[36] GRR was employed to form a Pd-rich layer on the surface of Cu nanoparticles, producing a Cu@Pd core@shell structure. In addition, Chen's group[47] prepared a Pt−W alloy by high-temperature annealing of Pt and W precursors under a reducing atmosphere and observed a negative alloy formation energy in density functional theory calculations, where a Pt-rich surface was formed due to strong surface segregation.

GRR is an effective method in the preparation of functional nanomaterials based on self-sacrificial templates. In essence, the substrate metal is corroded when a noble metal precursor is added and deposited. They act analogously to a nanogalvanic cell. The first metal with a lower standard electrode potential is the anode and will be readily oxidized by the noble metal precursors. Sacrificial consumption of the substrate results in the formation of smaller-sized metal nanoparticles. In this study, amorphous W nanoparticles were prepared and deposited on carbon support and used as the sacrificial substrate for GRR with a Pd(II) precursor, due to the marked discrepancy between the standard electrode potentials of W and Pd in alkaline media. As Pd in Pd−W alloy system tends to segregate to the surface, a Pd-rich surface will be produced, forming a W core@Pd shell structure, a unique feature that may be exploited for enhanced electrocatalytic performance.[48] It should be noted that studies of GRR on amorphous substrate materials have been scarce. Experimentally, it was found that during the GRR, the large W nanoparticles were indeed broken up into a number of markedly smaller nanoparticles. Upon thermal annealing under a reducing atmosphere, a quasi-core−shell structure was produced, where the core was rich in W and the shell in Pd (W@Pd NPs), most likely due to surface segregation of the elements, as manifested in scanning transmission electron microscopy (STEM) and elemental mapping analysis. The obtained W@Pd NPs were carefully characterized by a range of experimental techniques, such as transmission electron microscopy (TEM; including high-angle annular dark-field scanning transmission electron microscopy, HAADF-STEM), energy-dispersive X-ray spectroscopy (EDS), X-ray diffraction (XRD), and X-ray photoelectron spectroscopy (XPS). The evolution of the shape and size of the nanoparticles during the GRR process was monitored by STEM measurements, where the size and shape of the metal nanoparticles and the distribution of the nanoparticles on the carbon surface were found to be closely related to the reaction temperature. A galvanic cell model was constructed to account for the replacement reaction. The electrocatalytic performance toward EOR was then evaluated by cyclic voltammetry, chronoamperometry, as well as CO stripping voltammetry measurements. The sample prepared at 0 °C (W@Pd/C-0) was found to exhibit markedly better EOR activity than those prepared at higher temperatures (e.g., 25 and 50 °C), with a mass activity over 3 times that of commercial Pd/C and significantly better stability.

EXPERIMENTAL SECTION

Chemicals. Vulcan XC-72R carbon black was obtained from Cabot Co. and dried in vacuum at 80 °C before use to remove adsorbed water. Potassium tetrachloropalladate (K_2PdCl_4, ≥98%), tungsten hexacarbonyl ($W(CO)_6$, ≥99.9%), sodium hydroxide (NaOH, GR, ≥97%), and *o*-dichlorobenzene (≥99%) were purchased from Aladdin Co. Ethanol absolute (GR, ≥99.8%) was obtained from Sinopharm Chemical Reagents. All chemicals were used without further treatment. Water was supplied by a Milli-Q water purification system (18.2 MΩ·cm).

Synthesis of Carbon-Supported Tungsten Nanoparticles (W/C). W/C was prepared by the growth of amorphous tungsten on carbon black via thermal decomposition of $W(CO)_6$ in *o*-dichlorobenzene. In brief, 85 mg of $W(CO)_6$ and 80 mg of carbon black were dispersed into 50 mL of *o*-dichlorobenzene in a 250 mL three-neck flask by sonication for 45 min. The solution was then purged with N_2 for 1 h under vigorous stirring and refluxed at 180 °C for 12 h. After being cooled down naturally to room temperature, the product was obtained by vacuum filtration, rinsed with a copious amount of anhydrous ethanol, and dried in a vacuum oven at 60 °C overnight. Finally, the obtained sample was ground and heated in a tube furnace under a nitrogen atmosphere at 300 °C for 3 h. The resulted powder was referred to as W/C.

Synthesis of Carbon-Supported Quasi-Tungsten Core@Palladium Shell Nanoparticles (W@Pd/C). W@Pd/C was prepared by GRR of W/C with K_2PdCl_4. Typically, 40 mg of W/C obtained above was dispersed into 100 mL of Milli-Q water in a 250 mL three-neck flask, along with 5 drops of a 1 M NaOH solution under vigorous stirring and sonication for 1 h. The mixture was then chilled to 0 °C in an ice/water bath, into which 3.8 mL of a 20 M K_2PdCl_4 solution was added dropwise by an injection pump at 0.063 mL/min for 1 h. After the dripping was complete, the solution was kept in the ice/water bath under stirring for another 1 h and then warmed up to 25 °C. Subsequently, the suspension was filtered and rinsed extensively with Milli-Q water to remove excess Pd(II) precursor and then dried overnight in a vacuum oven at 60 °C. Finally, the produced sample was heated in a tube furnace under a He/H_2 atmosphere (20 vol % H_2 in He) at 250 °C for 3 h to induce the surface enrichment of Pd. The obtained result was denoted as W@Pd/C-0.

DOI: 10.1021/acsami.9b10156
ACS Appl. Mater. Interfaces 2019, 11, 30968−30976

Two additional samples were synthesized in the same fashion, except that the GRR was carried out at 25 and 50 °C. The corresponding samples were denoted as W@Pd/C-25 and W@Pd/C-50, respectively.

Structural Characterization. TEM studies were carried out with a JEOL JEM-2100F electron microscope. XRD patterns were acquired with a Bruker D8 advance diffractometer. XPS analyses were conducted on a Perkin-Elmer PHI-5000C ECSA system with Mg K_α radiation (1253.6 eV). Inductively coupled plasma-atomic emission spectroscopic (ICP-AES) measurements were carried out with a Hitachi P-4010 instrument.

Electrochemistry. Electrochemical measurements were carried out in a traditional three-electrode configuration with a CHI660E electrochemical workstation. A saturated calomel electrode (SCE) was used as the reference electrode and a Pt foil as the counter electrode. To prepare the working electrode, 2.0 mg of the W@Pd/C catalysts obtained above, 0.7 mL of C_2H_5OH, 0.3 mL of Milli-Q water, and 120 μL of Nafion were mixed under sonication to produce a catalyst ink, and 5.6 μL of the ink was dropcast onto a freshly polished glassy carbon electrode (GCE, d. 3 mm). CO-stripping experiment was carried out in a 1 M NaOH solution at the potential sweep rate of 10 mV s^{-1}. EOR studies were performed in an electrolyte solution of 1 M NaOH or 1 M NaOH +1 M C_2H_5OH, which was purged with ultrahigh-purity nitrogen for ca. 20 min and covered with a nitrogen atmosphere during data acquisition.

RESULTS AND DISCUSSION

In the W/C sample, amorphous tungsten nanoparticles were deposited onto the carbon support and showed an irregular shape and about 10−30 nm in length (Figure 1a). Upon the addition of a Pd(II) precursor, GRR occurred, where Pd atoms were deposited onto the W nanoparticle surface; meanwhile, dissolution of the W substrate as a sacrificial anode significantly reduced the size of the nanoparticles, which led to the formation of surface Pd-enriched W@Pd NPs. For the W@Pd/C-0 sample, the obtained nanoparticles exhibited no apparent agglomeration and were uniformly distributed on the carbon substrate surface (Figure 1b,c and Figure S1a), with an average diameter (3.31 nm, Figure 1b inset) markedly smaller than those of the original W nanoparticles and commercial Pd/C (ca. 3.9 nm in diameter, Figure S2). Selected area electron diffraction (SAED) measurements (inset to Figure 1c) show that the W@Pd/C-0 sample was polycrystalline in nature. In high-resolution TEM measurements (Figure 1d,e), one can see that the sample exhibits two sets of clearly defined lattice fringes. The low-contrast background shows somewhat curly lattice fringes, consistent with the C(002) planes, whereas the dark-contrast nanoparticles exhibit a lattice spacing of ca. 0.233 nm, somewhat larger than the interplanar spacing of the Pd(111) crystalline planes (no. 65−6174). The dilation of the palladium lattice spacing is likely due to the partial incorporation of heteroatom (W atom) into the Pd shell.[31,49] The related fast-Fourier transformed (FFT) patterns are depicted in the inset to Figure 1e, where the single crystalline nature of the nanoparticles can be clearly seen. HAADF-STEM and elemental mapping measurements in Figure S1 further confirm the successful formation of Pd-W bimetallic nanoparticles due to GRR of Pd(II) precursor with W nanoparticles.[48] From the bright-field STEM images in the left part of Figure 1f, the nanoparticles can be seen to exhibit apparent elemental segregation. The dark-contrast core is most likely W, whereas the surface layer shows a lighter contrast and is mostly likely Pd (left part of Figure 1f). This can be better illustrated by colored bright-field STEM images in the right part of Figure 1f (which was derived by adjusting the gray scale with DigitalMicrograph software) and manifested in EDS line scan (Figure 1g), where the W signals are markedly stronger in zones (I) and (II).

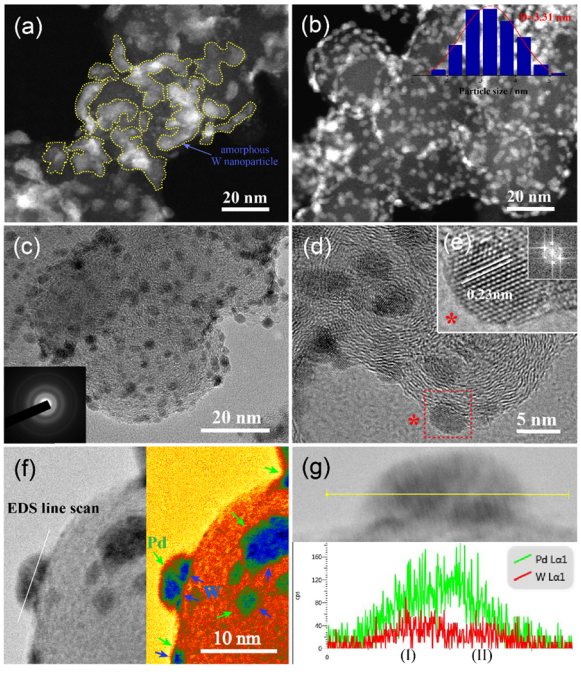

Figure 1. (a) HAADF-STEM image of W/C. The yellow lines represent the boundary between amorphous W nanoparticles. (b) HAADF-STEM image of W@Pd/C-0. Inset to (b) is the core size histogram of W@Pd NPs on the carbon surface. (c) TEM images of the W@Pd/C-0. Inset to (c) is the corresponding SAED patterns. (d) HRTEM image of the W@Pd/C-0. (e) Magnified HRTEM image of a single W@Pd nanoparticle. Inset to (e) is the corresponding FFT patterns. (f) Bright-field STEM image and colored STEM image of W@Pd/C-0. (g) EDS line scan of the single nanoparticle in (f).

Such a dramatic morphological evolution from W/C to W@Pd/C-0 was examined by HAADF-STEM measurements at different reaction time intervals, as demonstrated in Figure 2. One can see that that the original W/C nanoparticles were irregular in shape (Figure 2a). When 50% of the Pd(II) precursor was added, the number of nanoparticles increased significantly and the nanoparticle size was notably reduced (Figure 2b). The spherical shape of the nanoparticles became better defined when the reaction was warmed up to 25 °C, with the size reduced to 3−5 nm (Figure 2c). After 10 h GRR at 25 °C, Pd was enriched on the NP surface, and the boundary of the nanoparticles became apparently defined (Figure 2d). Subsequent thermal annealing under a He/H_2 atmosphere increased the crystallinity of the nanoparticles and facilitated the surface enrichment of Pd. Based on results from EDS analysis, the metal contents of W@Pd/C-0 were estimated to be 73.27 atom % Pd and 26.73 atom % W (pie charts in Figure 2).

Notably, when the GRR was carried out at higher temperatures (25 and 50 °C), the resulting nanoparticles showed a larger size, along with an increasing degree of agglomeration, which was likely due to enhanced GRR kinetics (Figure S3).

The crystallinity of the obtained samples was then characterized by XRD measurements. From Figure 3a, one can see that W/C shows only a broad peak centered at ca. 52°, signifying a mostly amorphous state of the sample. As for W@

DOI: 10.1021/acsami.9b10156
ACS Appl. Mater. Interfaces 2019, 11, 30968−30976

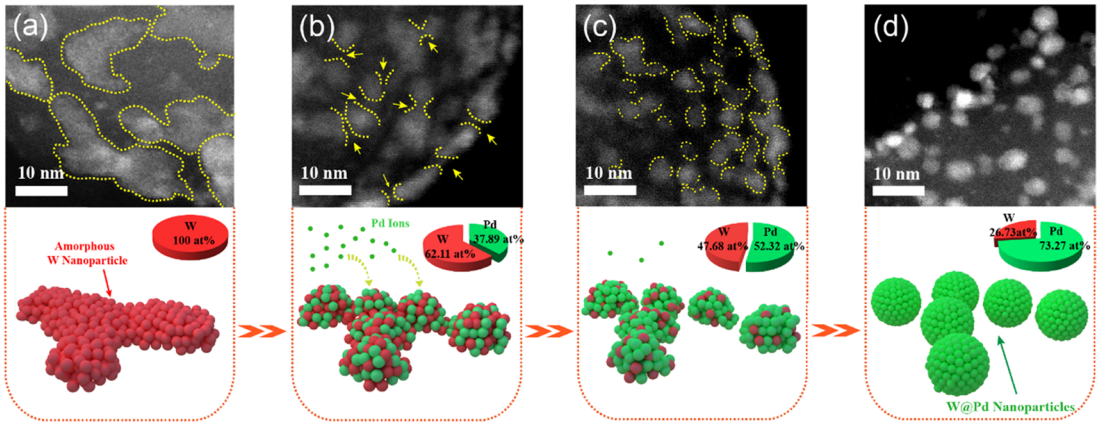

Figure 2. HAADF-STEM studies of the preparation of W@Pd/C-0. (a) W/C (before the start of GRR). (b) After the addition of 50% of the Pd(II) precursor. (c) After the addition of 100% of the Pd(II) precursor and the solution was warmed up to 25 °C. (d) Final sample that was obtained after thermal treatment at 250 °C. The pie charts below the STEM images show the corresponding relative content of Pd and W elements by EDS measurements. At the bottom is the schematic illustration of the GRR process.

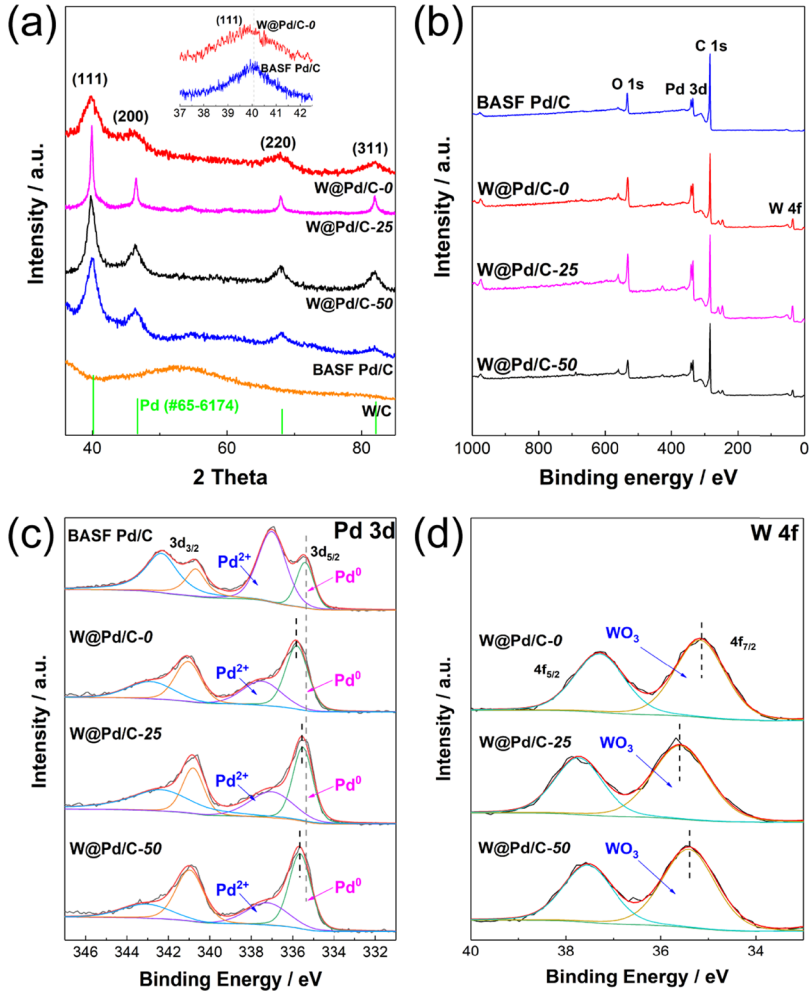

Figure 3. (a) XRD patterns of W@Pd/C-0, W@Pd/C-25, W@Pd/C-50, BASF Pd/C, and W/C. The inset to (a) is the zoom in within the 2θ range of 37° to 42.5° for the W@Pd/C-0 and BASF Pd/C samples. (b) Survey XPS spectra of BASF Pd/C, W@Pd/C-0, W@Pd/C-25, and W@Pd/C-50. (c) High-resolution spectra of the Pd 3d electrons of BASF Pd/C, W@Pd/C-0, W@Pd/C-25, and W@Pd/C-50. (d) High-resolution scan of the W 4f electrons of W@Pd/C-0, W@Pd/C-25, and W@Pd/C-50. Black curves in (c) and (d) are experimental data whereas colored ones are deconvolution fits.

Pd/C-0, W@Pd/C-25, W@Pd/C-50, and BASF Pd/C, four major peaks can be identified at 2θ = 40.1°, 46.7°, 68.2°, and 82.1°, which are the characteristic diffractions of the (111), (200), (220), and (311) planes of fcc Pd (no. 65−6174). As compared to commercial Pd/C, the W@Pd/C-0 sample exhibited somewhat broadened diffraction patterns, due to a

DOI: 10.1021/acsami.9b10156
ACS Appl. Mater. Interfaces 2019, 11, 30968−30976

reduced nanoparticle size (Figure 1); whereas for W@Pd/C-25 and W@Pd/C-50, the diffraction peaks are dramatically sharper, consistent with its larger particle sizes, as revealed in TEM measurements (Figure S3d,e). Additionally, one can see that the main (111) diffraction peak for W@Pd/C-0 shifted slightly in the negative direction, which suggests that a slightly expanded Pd lattice, most likely because of the incorporation of W into the Pd surface layer, in agreement with TEM results (Figure 1e).

XPS analyses were then carried out to evaluate the elemental composition and charge state of the samples. Figure 3b depicts the survey spectra of the W@Pd/C-0, W@Pd/C-25, W@Pd/C-50, and BASF Pd/C samples, where the elements of Pd, C, and O can be clearly identified in both samples (with W only in W@Pd/C). The absence of other elements indicates high purity of the samples. Additionally, on the basis of the integrated peak areas, the atomic ratio of Pd:W was estimated to be 3.5:1 for W@Pd/C-0, which is higher than that (2.7:1) obtained from EDS measurements, suggesting a Pd-enriched surface in the nanoparticles. High-resolution spectra of the Pd 3d and W 4f electrons in W@Pd/C-0, W@Pd/C-25, W@Pd/C-50, and BASF Pd/C are displayed in Figure 3c,d. For the W@Pd/C-0 sample, deconvolution yields a peak at 335.8 eV, consistent with that for Pd(0) $3d_{5/2}$ electrons; and for W@Pd/C-25 and W@Pd/C-50, the Pd(0) $3d_{5/2}$ binding energy was slightly lower at 335.5 eV and 335.7 eV, respectively. Note that these are all somewhat greater than that (335.4 eV) of BASF Pd/C.[50−52] Deconvolution of the W@Pd/C-0 spectrum also yields a second peak at 337.3 eV, suggesting the formation of Pd(II) species; and the content of Pd(II) for W@Pd/C-0, W@Pd/C-25, W@Pd/C-50, and BASF Pd/C catalysts was estimated to be 27.9%, 28.0%, 27.3%, and 70.3%, respectively. This suggests that Pd/C is prone to oxidation in ambient conditions, whereas in the alloy nanoparticles, Pd oxidation was substantially suppressed.

From the high-resolution W 4f spectra in Figure 3d, W@Pd/C-0 can be seen to exhibit a doublet at 37.3 and 35.2 eV, which can be attributed to WO_3.[53] The fact that no metallic W was observed is likely due to the consumption of W(0) during GRR, which led to the breakup of the nanoparticles into much smaller ones. Interestingly, the W^{6+} $4f_{7/2}$ binding energy increased to 35.6 eV for W@Pd/C-25 and 35.4 eV for W@Pd/C-50. This suggests that, in conjunction with the variation of the Pd(0) $3d_{5/2}$ binding energy, the charge transfer from Pd to W likely occurred and became intensified in the order of W@Pd/C-25, W@Pd/C-50, and W@Pd/C-0.

The electrocatalytic activity of W@Pd/C-0, W@Pd/C-25, and W@Pd/C-50 toward EOR were then assessed in alkaline media, using BASF Pd/C as the benchmark material. The loading of Pd in the above catalysts was listed in Table 1 and the palladium mass was used to normalize the current density (mass activity). CV curves were first acquired in nitrogen-saturated 1 M NaOH (Figure 4a). A pair of well-defined current peaks emerged in the low potential range of −1.0 to −0.7 V in all CVs, due to hydrogen adsorption/desorption,[54] and the cathodic peaks at ca. −0.34 V arose from the reduction of PdO_x. Notably, W@Pd/C-0 exhibited substantially stronger Pd oxidation/reduction and hydrogen adsorption/desorption than BASF Pd/C, W@Pd/C-25, and W@Pd/C-50. In the anodic potential scan, a PdO_x monolayer was formed on the nanoparticle surface. Hence, a considerably higher cathodic wave of W@Pd/C-0 means a markedly larger number of exposed Pd active sites, in comparison to other samples in the series. From these voltammetric data, the effective electrochemical surface area can be seen to diminish in the order of W@Pd-0 > W@Pd-25 > W@Pd/C-50, in coincidence with the increasing agglomeration of the nanoparticles (Figure 1 and Figures S2 and S3).

Table 1. Compositional Analysis of W@Pd/C-0, W@Pd/C-25, W@Pd/C-50, and BASF Pd/C Catalysts by XPS, EDS, and ICP-AES Measurements

catalyst	W@Pd/C-0	W@Pd/C-25	W@Pd/C-50	BASF Pd/C
Pd:W atomic ratio (by XPS)	3.5:1	2.5:1	3.3:1	
Pd:W atomic ratio (by EDS)	2.7:1	3.3:1	3.1:1	
Pd loading wt % (by ICP-AES)	14.2	15.7	15.5	38.9

The EOR performance of these Pd-based catalysts was then examined in the 1.0 M NaOH +1.0 M C_2H_5OH solution. As shown in Figure 4b, these catalysts all exhibited a pair of anodic peaks. In the forward scan (−0.3 V to −0.1 V), one can see an anodic peak at −0.21 V due to the ethanol oxidation into intermediate products such as $CH_3C^*{=}O$, CH_x, and CO_{ad};[55] and in the reverse scan, an anodic peak also appeared owing to the further oxidation of these intermediate species.[56,57] From the peak current density, one can see that the W@Pd/C-0 catalyst possessed a remarkable mass activity of 9535.5 mA mg_{Pd}^{-1}, which is over 3 times better than those of BASF Pd/C (2877.4 mA mg_{Pd}^{-1}), W@Pd/C-25 (2911.3 mA mg_{Pd}^{-1}), and W@Pd/C-50 (2726.6 mA mg_{Pd}^{-1} (Figure 4b inset). In fact, the EOR performance of W@Pd/C-0 is even better than leading results reported recently in the literature (Table S1).

The observed EOR activity can be correlated with results from XPS measurements. As depicted in Figure 3b−d, the Pd 3d binding energy of the W@Pd/C-0 sample exhibited a marked blue shift, as compared to the others in the series, suggesting a lower Pd core-level as compared to the Fermi level, due to the incorporation of the W species. Such a decline of the Pd d-band center is anticipated to weaken the interactions with EOR reaction intermediates.[10,32] Note that for EOR in alkaline media, the removal of the adsorbed species is the rate-limiting step, and an appropriate drop of the d-band center leads to weakened adsorption of both the reactants and intermediates in a moderate manner, and hence enhanced EOR activity.[8,19]

The surface properties of the W@Pd/C-0, W@Pd/C-25, W@Pd/C-50, and BASF Pd/C nanoparticles were then evaluated and compared by CO stripping measurements. With a pre-adsorbed CO monolayer at −0.8 V (vs SCE) in 1 M NaOH (Figure 4c), one can see that the onset potential of CO oxidation was the most negative for the W@Pd/C-0 sample, along with the greatest oxidation peak current among the series, indicating that CO can be more easily oxidized on W@Pd/C-0 than others, such that the catalyst surface possessed a higher number of active sites. In fact, by integrating the charge of the anodic CO stripping peak,[58] the corresponding electrochemical surface areas (ECSA) was estimated to be 157.8 $m^2mg_{Pd}^{-1}$ for W@Pd/C-0, 42.3 $m^2mg_{Pd}^{-1}$ for W@Pd/C-25, 40.9 $m^2mg_{Pd}^{-1}$ for W@Pd/C-50, and 41.2 $m^2mg_{Pd}^{-1}$ for BASF Pd/C.

DOI: 10.1021/acsami.9b10156
ACS Appl. Mater. Interfaces 2019, 11, 30968−30976

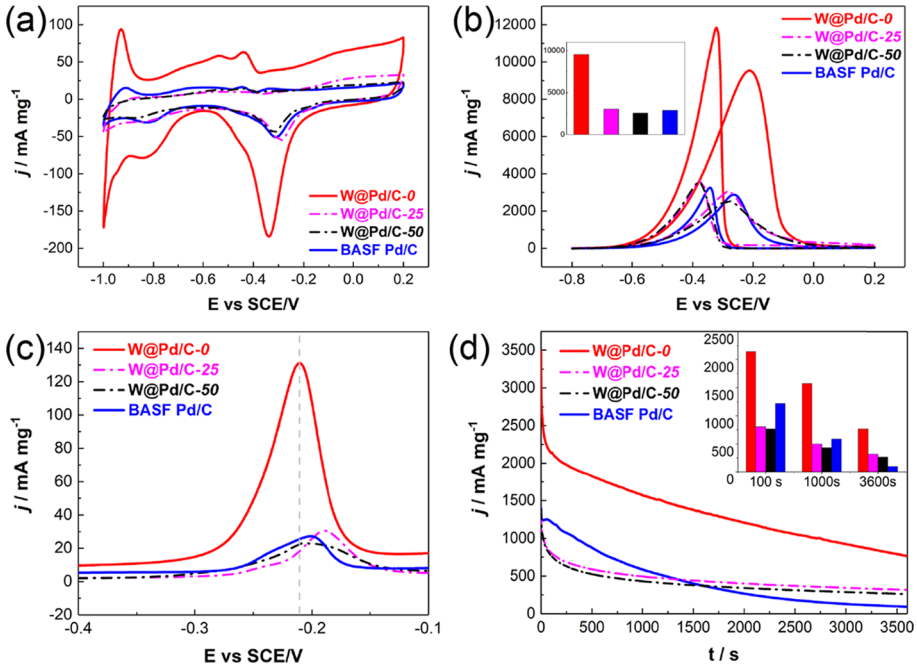

Figure 4. (a) CVs of the W@Pd/C-0, W@Pd/C-25, W@Pd/C-50, and BASF Pd/C catalysts in 1.0 M NaOH solution at the sweep rate of 50 mV s^{-1}. (b) Cyclic voltammograms of W@Pd/C-0, W@Pd/C-25, W@Pd/C-50, and BASF Pd/C catalysts in 1.0 M NaOH +1.0 M C_2H_5OH at the sweep rate of 50 mV s^{-1}. Panel (b) inset is the comparison of the peak current densities of the various catalysts. (c) CO stripping curves for W@Pd/C-0, W@Pd/C-25, W@Pd/C-50, and BASF Pd/C in 1.0 M NaOH at the sweep rate of 10 mV s^{-1}. (d) Chronoamperometric profiles of W@Pd/C-0, W@Pd/C-25, W@Pd/C-50, and BASF Pd/C in 1.0 M NaOH +1.0 M C_2H_5OH at the electrode potential of −0.35 V (vs SCE). Panel (d) inset is the comparison of the current densities of the various catalysts after EOR durability studies for up to 3600 s.

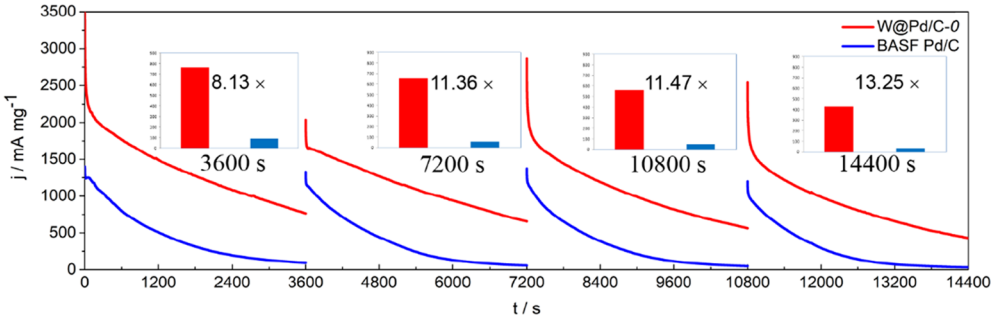

Figure 5. Long-time durability tests of W@Pd/C-0 and BASF Pd/C at the applied potential of −0.35 V (vs SCE). At 3600, 7200, and 10800 s, the catalysts were reactivated and the electrolyte was replaced. Insets show the corresponding current densities for W@Pd/C-0 and BASF Pd/C at 3600, 7200, 10800, and 14400 s.

Furthermore, Figure S4 shows the CVs of W@Pd/C-0 before and after annealing. The mass activity of EOR was estimated to be 7258.7 mA mg_{Pd}^{-1} before annealing and increased by about 31.3% after annealing, likely due to the formation of an increasing number of active sites. To examine the stability of W@Pd/C-0, chronoamperometric (i−t) tests were carried out and compared in the 1 M NaOH +1.0 C_2H_5OH solution at the applied potential of −0.35 V for 3600 s. From Figure 4d and inset, one can see that whereas all four samples show an apparent diminishment of the EOR current densities (the decay is particularly rapid within the first 100 s, likely due to poisoning of carbonaceous intermediates during the continuous electro-oxidation of ethanol); the W@Pd/C-0 catalyst shows markedly higher current densities within the entire test period than W@Pd/C-25, W@Pd/C-50, and commercial BASF Pd/C, signifying enhanced stability. For instance, after continuous operation for 3600 s, the current density of W@Pd/C-0 is ca. 763 mA mg^{-1}, which is 8.1, 2.4, and 2.9 times that of W@Pd/C-25 (317 mA mg^{-1}), W@Pd/C-50 (262 mA mg^{-1}), and BASF Pd/C (94 mA mg^{-1}), respectively. This corresponds to a retention of the current density (j_{3600}/j_{100}) on W@Pd/C-0, W@Pd/C-25, W@Pd/C-50, and BASF Pd/C at 35.7, 39.5, 34.2. and 7.7%, respectively.

To further investigate the long-term durability of the catalysts, chronoamperometric measurements of W@Pd/C-0 and BASF Pd/C were carried out and compared at the potential of −0.35 V for 4 h. The working electrode was reactivated after every 3600 s by switching the electrolyte to a fresh 1 M NaOH solution and running 5 CV cycles. This CV cleaning process helped remove carbonaceous intermediates adsorbed on the catalyst surface and recover its electrocatalytic activity. Reactivated working electrode was then subjected to another 3600 s for a chronoamperometric test in a fresh 1.0 M NaOH +1.0 M C_2H_5OH solution. Figure 5 shows a four-segment electrochemical curve, and the histograms in the figure insets show the current densities of W@Pd/C-0 and

DOI: 10.1021/acsami.9b10156
ACS Appl. Mater. Interfaces 2019, 11, 30968−30976

BASF Pd/C at the end of each segment. At 3600 s, W@Pd/C-0 exhibited a current density that was over 8 times that of BASF Pd/C. As the operation time was extended to 14400 s, this ratio increased to 13.25, indicating marked enhancement of the stability as compared to Pd/C.[48]

CONCLUSIONS

In summary, W@Pd core−shell nanoparticles were produced by GRR of amorphous W nanoparticles with a Pd(II) precursor, where the resulting nanoparticles were markedly smaller in size than the starting W nanoparticles. STEM measurements showed a Pd-rich surface of the resulting nanoparticles, where the morphological evolution could be controlled by reaction temperature. XPS measurements showed that the charge transfer from Pd to W increased in the order of W@Pd/C-25 < W@Pd/C-50 < W@Pd/C-0. Electrochemically, W@Pd/C-0 outperformed others in the series, with an EOR activity over three times better than that of BASF Pd/C, owing to a large surface area that was derived from the reduced size and uniform deposition of W@Pd NPs, ready accessibility of active sites resulting from the dissolution of near-surface tungsten species and reduced consumption of Pd. These results suggest a new strategy for the facile synthesis of advanced nanoscale electrocatalysts for fuel cell electrochemistry.

ASSOCIATED CONTENT

Supporting Information

The Supporting Information is available free of charge on the ACS Publications website at DOI: 10.1021/acsami.9b10156.

Reaction model of different temperature and additional TEM images of W@Pd/C-25, W@Pd/C-50 W@Pd/C-0, and commercial Pd/C (PDF)

AUTHOR INFORMATION

Corresponding Authors

*E-mail: liqiaoxia@shiep.edu.cn (Q.L.).
*E-mail: Shaowei@ucsc.edu (S.C.).

ORCID

Shaowei Chen: 0000-0002-3668-8551

Notes

The authors declare no competing financial interest.

ACKNOWLEDGMENTS

We sincerely thank Prof. W.-B. Cai for his insightful comments. This study was supported by the National Science Foundation of China (91745112), the Key Project of Shanghai Committee of Science and Technology, China (15DZ1206902), and the Science and Technology Commission of Shanghai Municipality, China (18020500800). S.W.C. thanks the National Science Foundation for partial support of the work (CHE-1710408 and CHE-1900235). Q.X.L. is supported by a research fellowship from the Shanghai Municipal Education Commission.

REFERENCES

(1) Stephens, I. E. L.; Rossmeisl, J.; Chorkendorff, I. Toward Sustainable Fuel Cells. *Science* **2016**, *354*, 1378−1379.

(2) Wang, F.; Xue, H.; Tian, Z.; Xing, W.; Feng, L. Fe2P as a Novel Efficient Catalyst Promoter in Pd/C System for Formic Acid Electro-Oxidation in Fuel Cells Reaction. *J. Power Sources* **2018**, *375*, 37−42.

(3) Zhang, G.; Yang, Z.; Zhang, W.; Wang, Y. Nanosized Mo-doped CeO2enhances the Electrocatalytic Properties of the Pt Anode Catalyst in Direct Methanol Fuel Cells. *J. Mater. Chem. A* **2017**, *5*, 1481−1487.

(4) Li, Z.; Lin, R.; Liu, Z.; Li, D.; Wang, H.; Li, Q. Novel Graphitic Carbon Nitride/Graphite Carbon/Palladium Nanocomposite as a High-Performance Electrocatalyst for the Ethanol Oxidation Reaction. *Electrochim. Acta* **2016**, *191*, 606−615.

(5) Yue, H.; Zhao, Y.; Ma, X.; Gong, J. Ethylene Glycol: Properties, Synthesis, and Applications. *Chem. Soc. Rev.* **2012**, *41*, 4218−4244.

(6) An, L.; Zhao, T. S. Transport Phenomena in Alkaline Direct Ethanol Fuel Cells for Sustainable Energy Production. *J. Power Sources* **2017**, *341*, 199−211.

(7) Liu, M.; Zhang, R.; Chen, W. Graphene-Supported Nanoelectrocatalysts for Fuel Cells: Synthesis, Properties, and Applications. *Chem. Rev.* **2014**, *114*, 5117−5160.

(8) Wang, Y.; Zou, S.; Cai, W.-B. Recent Advances on Electro-Oxidation of Ethanol on Pt- and Pd-Based Catalysts: From Reaction Mechanisms to Catalytic Materials. *Catalysts* **2015**, *5*, 1507−1534.

(9) Chen, L.; Lu, L.; Zhu, H.; Chen, Y.; Huang, Y.; Li, Y.; Wang, L. Improved Ethanol Electrooxidation Performance by Shortening Pd−Ni Active Site Distance in Pd−Ni−P Nanocatalysts. *Nat. Commun.* **2017**, *8*, 14136−14144.

(10) Li, C.; Yuan, Q.; Ni, B.; He, T.; Zhang, S.; Long, Y.; Gu, L.; Wang, X. Dendritic Defect-Rich Palladium−Copper−Cobalt Nanoalloys as Robust Multifunctional Non-Platinum Electrocatalysts for Fuel Cells. *Nat. Commun.* **2018**, *9*, 3702−3710.

(11) Hernandez-Fernandez, P.; Masini, F.; McCarthy, D. N.; Strebel, C. E.; Friebel, D.; Deiana, D.; Malacrida, P.; Nierhoff, A.; Bodin, A.; Wise, A. M.; Nielsen, J. H.; Hansen, T. W.; Nilsson, A.; Stephens, I. E. L.; Chorkendorff, I. Mass-Selected Nanoparticles of PtxY as Model Catalysts for Oxygen Electroreduction. *Nat. Chem.* **2014**, *6*, 732−738.

(12) Gan, L.; Rudi, S.; Cui, C.; Heggen, M.; Strasser, P. Size-Controlled Synthesis of Sub-10 nm PtNi3 Alloy Nanoparticles and their Unusual Volcano-Shaped Size Effect on ORR Electrocatalysis. *Small* **2016**, *12*, 3189−3196.

(13) Wu, T.; Fan, J.; Li, Q.; Shi, P.; Xu, Q.; Min, Y. Palladium Nanoparticles Anchored on Anatase Titanium Dioxide-Black Phosphorus Hybrids with Heterointerfaces: Highly Electroactive and Durable Catalysts for Ethanol Electrooxidation. *Adv. Energy Mater.* **2018**, *8*, 1701799−1701809.

(14) Liu, Q.; Jiang, K.; Fan, J.; Lin, Y.; Min, Y.; Xu, Q.; Cai, W.-B. Manganese Dioxide Coated Graphene Nanoribbons Supported Palladium Nanoparticles as an Efficient Catalyst for Ethanol Electrooxidation in Alkaline Media. *Electrochim. Acta* **2016**, *203*, 91−98.

(15) Yang, Y.; Li, Y.-H.; Zhao, Y.-F.; Li, P.-W.; Li, Q.-X. Pd/WO3/C Nanocomposite with APTMS-functionalized Tungsten Oxide Nanosheet for Formic Acid Electrooxidation Enhancement. *J. Nanopart. Res.* **2018**, *20*, 12−19.

(16) Bianchini, C.; Shen, P. K. Palladium-Based Electrocatalysts for Alcohol Oxidation in Half Cells and in Direct Alcohol Fuel Cells. *Chem. Rev.* **2009**, *109*, 4183−4206.

(17) Akhairi, M. A. F.; Kamarudin, S. K. Catalysts in Direct Ethanol Fuel Cell (DEFC): An Overview. *Int. J. Hydrogen Energy* **2016**, *41*, 4214−4228.

(18) Antolini, E. Catalysts for Direct Ethanol Fuel Cells. *J. Power Sources* **2007**, *170*, 1−12.

(19) Kibler, L. A.; El-Aziz, A. M.; Hoyer, R.; Kolb, D. M. Tuning Reaction Rates by Lateral Strain in a Palladium Monolayer. *Angew. Chem., Int. Edit.* **2005**, *44*, 2080−2084.

(20) Wang, C.; Zhang, Y.; Zhang, Y.; Xu, P.; Feng, C.; Chen, T.; Guo, T.; Yang, F.; Wang, Q.; Wang, J.; Shi, M.; Fan, L.; Chen, S. Highly Ordered Hierarchical Pt and PtNi Nanowire Arrays for Enhanced Electrocatalytic Activity toward Methanol Oxidation. *ACS Appl. Mater. Interfaces* **2018**, *10*, 9444−9450.

(21) Liu, P.; Nørskov, J. K. Ligand and Ensemble Effects in Adsorption on Alloy Surfaces. *Phys. Chem. Chem. Phys.* **2001**, *3*, 3814−3818.

(22) Kitchin, J. R.; Nørskov, J. K.; Barteau, M. A.; Chen, J. G. Role of Strain and Ligand Effects in the Modification of the Electronic and

DOI: 10.1021/acsami.9b10156
ACS Appl. Mater. Interfaces 2019, 11, 30968−30976

Chemical Properties of Bimetallic Surfaces. *Phys. Rev. Lett.* **2004**, *93*, 156801−156804.
(23) Lee, Y. W.; Kim, M.; Kim, Y.; Kang, S. W.; Lee, J.-H.; Han, S. W. Synthesis and Electrocatalytic Activity of Au−Pd Alloy Nanodendrites for Ethanol Oxidation. *J. Phys. Chem. C* **2010**, *114*, 7689−7693.
(24) Bi, C.; Song, Y.; He, H.; Wu, C.; Du, W.; Huang, L.; Moehwald, H.; Xia, H. Simple Synthesis and Surface Facet-Tuning of Ultrathin Alloy-Shells of Au@AuPd Nanoparticles via Silver-Assisted Co-reduction onto Facet-controlled Au Nanoparticles. *J. Mater. Chem. A* **2018**, *6*, 7675−7685.
(25) Guo, J.; Chen, R.; Zhu, F.-C.; Sun, S.-G.; Villullas, H. M. New Understandings of Ethanol Oxidation Reaction Mechanism on Pd/C and Pd2Ru/C Catalysts in Alkaline Direct Ethanol Fuel Cells. *Appl. Catal., B* **2018**, *224*, 602−611.
(26) Shen, S.; Guo, Y.; Wei, G.; Luo, L.; Li, F.; Li, L.; Xia, G.; Zhang, J. An Exploration of the Use of Au Submonolayer Decorated Pd7Ir Nanoparticles as a Highly Active Electrocatalyst for the Ethanol Oxidation Reaction in Alkaline Media. *Catal. Sci. Technol.* **2018**, *8*, 3465−3468.
(27) Ma, S.-Y.; Li, H.-H.; Hu, B.-C.; Cheng, X.; Fu, Q.-Q.; Yu, S.-H. Synthesis of Low Pt-Based Quaternary PtPdRuTe Nanotubes with Optimized Incorporation of Pd for Enhanced Electrocatalytic Activity. *J. Am. Chem. Soc.* **2017**, *139*, 5890−5895.
(28) Jiang, K.; Cai, W.-B. Carbon Supported Pd-Pt-Cu Nanocatalysts for Formic Acid Electrooxidation: Synthetic Screening and Componential Functions. *Appl. Catal., B* **2014**, *147*, 185−192.
(29) Sulaiman, J. E.; Zhu, S.; Xing, Z.; Chang, Q.; Shao, M. Pt-Ni Octahedra as Electrocatalysts for the Ethanol Electro-Oxidation Reaction. *ACS Catal.* **2017**, *7*, 5134−5141.
(30) Zhang, B.-W.; Sheng, T.; Wang, Y.-X.; Qu, X.-M.; Zhang, J.-M.; Zhang, Z.-C.; Liao, H.-G.; Zhu, F.-C.; Dou, S.-X.; Jiang, Y.-X.; Sun, S.-G. Platinum−Cobalt Bimetallic Nanoparticles with Pt Skin for Electro-Oxidation of Ethanol. *ACS Catal.* **2017**, *7*, 892−895.
(31) Wang, J.-Y.; Kang, Y.-Y.; Yang, H.; Cai, W.-B. Boron-Doped Palladium Nanoparticles on Carbon Black as a Superior Catalyst for Formic Acid Electro-oxidation. *J. Phys. Chem. C* **2009**, *113*, 8366−8372.
(32) Wang, Y.; Shi, F.-F.; Yang, Y.-Y.; Cai, W.-B. Carbon Supported Pd−Ni−P Nanoalloy as an Efficient Catalyst for Ethanol Electrooxidation in Alkaline Media. *J. Power Sources* **2013**, *243*, 369−373.
(33) Wang, Y.; Jiang, K.; Cai, W.-B. Enhanced Electrocatalysis of Ethanol on Dealloyed Pd-Ni-P Film in Alkaline Media: an Infrared Spectroelectrochemical Investigation. *Electrochim. Acta* **2015**, *162*, 100−107.
(34) Xu, H.; Yan, B.; Zhang, K.; Wang, C.; Zhong, J.; Li, S.; Yang, P.; Du, Y. Facile Synthesis of Pd-Ru-P Ternary Nanoparticle Networks with Enhanced Electrocatalytic Performance for Methanol Oxidation. *Int. J. Hydrogen Energy* **2017**, *42*, 11229−11238.
(35) Wang, A.-L.; Xu, H.; Feng, J.-X.; Ding, L.-X.; Tong, Y.-X.; Li, G.-R. Design of Pd/PANI/Pd Sandwich-Structured Nanotube Array Catalysts with Special Shape Effects and Synergistic Effects for Ethanol Electrooxidation. *J. Am. Chem. Soc.* **2013**, *135*, 10703−10709.
(36) Cai, J.; Zeng, Y.; Guo, Y. Copper@palladium−copper Core−shell Nanospheres as a Highly Effective Electrocatalyst for Ethanol Electro-oxidation in Alkaline media. *J. Power Sources* **2014**, *270*, 257−261.
(37) Huang, L.; Yang, J.; Wu, M.; Shi, Z.; Lin, Z.; Kang, X.; Chen, S. PdAg@Pd Core-shell Nanotubes: Superior Catalytic Performance Towards Electrochemical Oxidation of Formic Acid and Methanol. *J. Power Sources* **2018**, *398*, 201−208.
(38) Zhao, T.-T.; Wang, H.; Han, X.; Jiang, K.; Lin, H.; Xie, Z.; Cai, W.-B. A Comparative Investigation of Electrocatalysis at Pt Monolayers on Shape-controlled Au Nanocrystals: Facet Effect Versus Strain Effect. *J. Mater. Chem. A* **2016**, *4*, 15845−15850.
(39) Shao, M.; Chang, Q.; Dodelet, J.-P.; Chenitz, R. Recent Advances in Electrocatalysts for Oxygen Reduction Reaction. *Chem. Rev.* **2016**, *116*, 3594−3657.
(40) Chen, H.; Xing, Z.; Zhu, S.; Zhang, L.; Chang, Q.; Huang, J.; Cai, W.-B.; Kang, N.; Zhong, C.-J.; Shao, M. Palladium Modified Gold Nanoparticles as Electrocatalysts for Ethanol Electrooxidation. *J. Power Sources* **2016**, *321*, 264−269.
(41) Dai, C.; Yang, Y.; Zhao, Z.; Fisher, A.; Liu, Z.; Cheng, D. From Mixed to Three-layer Core/Shell PtCu Nanoparticles: Ligand-induced Surface Segregation to Enhance Electrocatalytic Activity. *Nanoscale* **2017**, *9*, 8945−8951.
(42) Papaderakis, A.; Mintsouli, I.; Georgieva, J.; Sotiropoulos, S. Electrocatalysts Prepared by Galvanic Replacement. *Catalysts* **2017**, *7*, 80−113.
(43) Xia, X.; Wang, Y.; Ruditskiy, A.; Xia, Y. 25th Anniversary Article: Galvanic Replacement: A Simple and Versatile Route to Hollow Nanostructures with Tunable and Well-Controlled Properties. *Adv. Mater.* **2013**, *25*, 6313−6333.
(44) Cobley, C. M.; Xia, Y. Engineering the Properties of Metal Nanostructures via Galvanic Replacement Reactions. *Mater. Sci. Engi., R* **2010**, *70*, 44−62.
(45) Zou, L.; Li, J.; Yuan, T.; Zhou, Y.; Li, X.; Yang, H. Structural Transformation of Carbon-supported Pt_3Cr Nanoparticles from a Disordered to an Ordered Phase as a Durable Oxygen Reduction Electrocatalyst. *Nanoscale* **2014**, *6*, 10686−10692.
(46) Chen, J.; Wiley, B.; McLellan, J.; Xiong, Y.; Li, Z.-Y.; Xia, Y. Optical Properties of Pd−Ag and Pt−Ag Nanoboxes Synthesized via Galvanic Replacement Reactions. *Nano Lett.* **2005**, *5*, 2058−2062.
(47) Dai, Y.; Ou, L.; Liang, W.; Yang, F.; Liu, Y.; Chen, S. Efficient and Superiorly Durable Pt-Lean Electrocatalysts of Pt−W Alloys for the Oxygen Reduction Reaction. *J. Phys. Chem. C* **2011**, *115*, 2162−2168.
(48) Ruban, A. V.; Skriver, H. L.; Nørskov, J. K. Surface Segregation Energies in Transition-metal Alloys. *Phys. Rev. B* **1999**, *59*, 15990−16000.
(49) Jiang, B.; Zhang, X.-G.; Jiang, K.; Wu, D.-Y.; Cai, W.-B. Boosting Formate Production in Electrocatalytic CO_2 Reduction over Wide Potential Window on Pd Surfaces. *J. Am. Chem. Soc.* **2018**, *140*, 2880−2889.
(50) Lu, L.; Shen, L.; Shi, Y.; Chen, T.; Jiang, G.; Ge, C.; Tang, Y.; Chen, Y.; Lu, T. New Insights into Enhanced Electrocatalytic Performance of Carbon Supported Pd−Cu Catalyst for Formic Acid Oxidation. *Electrochim. Acta* **2012**, *85*, 187−194.
(51) Kariuki, N. N.; Wang, X.; Mawdsley, J. R.; Ferrandon, M. S.; Niyogi, S. G.; Vaughey, J. T.; Myers, D. J. Colloidal Synthesis and Characterization of Carbon-Supported Pd−Cu Nanoparticle Oxygen Reduction Electrocatalysts. *Chem. Mater.* **2010**, *22*, 4144−4152.
(52) Wakisaka, M.; Mitsui, S.; Hirose, Y.; Kawashima, K.; Uchida, H.; Watanabe, M. Electronic Structures of Pt−Co and Pt−Ru Alloys for CO-Tolerant Anode Catalysts in Polymer Electrolyte Fuel Cells Studied by EC−XPS. *J. Phys. Chem. B* **2006**, *110*, 23489−23496.
(53) Hu, G.; Nitze, F.; Gracia-Espino, E.; Ma, J.; Barzegar, H. R.; Sharifi, T.; Jia, X.; Shchukarev, A.; Lu, L.; Ma, C.; Yang, G.; Wågberg, T. Small Palladium Islands Embedded in Palladium-Tungsten Bimetallic Nanoparticles form Catalytic Hotspots for Oxygen Reduction. *Nat. Commun.* **2014**, *5*, 5253−5261.
(54) Hoshi, N.; Nakamura, M.; Maki, N.; Yamaguchi, S.; Kitajima, A. Structural Effects on Voltammograms of the Low Index Planes of Palladium and Pd(S)-[n(100)×(111)] Surfaces in Alkaline Solution. *J. Electroanal. Chem.* **2008**, *624*, 134−138.
(55) Yang, Y.-Y.; Ren, J.; Li, Q.-X.; Zhou, Z.-Y.; Sun, S.-G.; Cai, W.-B. Electrocatalysis of Ethanol on a Pd Electrode in Alkaline Media: An in Situ Attenuated Total Reflection Surface-Enhanced Infrared Absorption Spectroscopy Study. *ACS Catal.* **2014**, *4*, 798−803.
(56) Chen, A.; Holt-Hindle, P. Platinum-Based Nanostructured Materials: Synthesis, Properties, and Applications. *Chem. Rev.* **2010**, *110*, 3767−3804.
(57) Xu, C. W.; Wang, H.; Shen, P. K.; Jiang, S. P. Highly Ordered Pd Nanowire Arrays as Effective Electrocatalysts for Ethanol Oxidation in Direct Alcohol Fuel Cells. *Adv. Mater.* **2007**, *19*, 4256−4259.

DOI: 10.1021/acsami.9b10156
ACS Appl. Mater. Interfaces 2019, 11, 30968−30976

(58) Shao, M.; Odell, J. H.; Choi, S.-I.; Xia, Y. Electrochemical Surface Area Measurements of Platinum- and Palladium-based Nanoparticles. *Electrochem. Commun.* **2013**, *31*, 46−48.

DOI: 10.1021/acsami.9b10156
ACS Appl. Mater. Interfaces 2019, 11, 30968−30976